Earth and Space Science

RESEARCH ARTICLE
10.1029/2022EA002465

Key Points:

- For the first time, an $M \sim 6$ earthquake sequence is in-depth analyzed in a focal zone, suggesting a transpressive stress regime
- The 2019 sequence and reinterpreted morphostructural data reveal recently activated faults
- Two mainshocks occurred as a doublet on nearly parallel faults oblique to the major Algeciras Fault System

Supporting Information:

Supporting Information may be found in the online version of this article.

Correspondence to:

E. Poveda,
hpoveda@sgc.gov.co

Citation:

Poveda, E., Pedraza, P., Velandia, F., Mayorga, E., Plicka, V., Gallovič, F., & Zahradník, J. (2022). 2019 Mw 6.0 Mesetas (Colombia) earthquake sequence: Insights from integrating seismic and morphostructural observations. *Earth and Space Science*, *9*, e2022EA002465. https://doi.org/10.1029/2022EA002465

Received 13 JUN 2022
Accepted 28 OCT 2022

Author Contributions:

Conceptualization: Esteban Poveda, Patricia Pedraza, Francisco Velandia, Jiří Zahradník
Formal analysis: Esteban Poveda, Patricia Pedraza, Francisco Velandia, František Gallovič, Jiří Zahradník
Investigation: Esteban Poveda, Patricia Pedraza, Edwin Mayorga
Methodology: Esteban Poveda, Patricia Pedraza, Edwin Mayorga, Vladimír Plicka, František Gallovič, Jiří Zahradník
Software: Vladimír Plicka, František Gallovič, Jiří Zahradník

2019 Mw 6.0 Mesetas (Colombia) Earthquake Sequence: Insights From Integrating Seismic and Morphostructural Observations

Esteban Poveda[1], Patricia Pedraza[1], Francisco Velandia[2], Edwin Mayorga[1], Vladimír Plicka[3], František Gallovič[3], and Jiří Zahradník[3]

[1]Servicio Geológico Colombiano, Dirección de Geoamenazas, Bogotá, Colombia, [2]Escuela de Geología, Universidad Industrial de Santander, Bucaramanga, Colombia, [3]Faculty of Mathematics and Physics, Charles University, Prague, Czech Republic

Abstract The boundary between the Northern Andean block and the South American plate is a first-order tectonic structure in Colombia with historically $M > 7$ earthquakes. However, details about individual sections of the system remain unknown. We illuminate the seismotectonic of the Algeciras fault by investigating an earthquake sequence that started on 24 December 2019. Using seismic networks at region, we estimate foreshocks and aftershocks focal mechanisms, local stress field, kinematic slip models of the largest events, and Coulomb stress changes. We integrate seismological and morphostructural observations to characterize source properties and reinterpret local faults. Two mainshocks (doublet of Mw 6.0 and 5.8) occurred within 16 min, rupturing just a few kilometers from each other. Discrimination of causative faults among the centroid moment-tensor nodal planes is difficult because the focal zone is a complex tectonic environment. The focal mechanisms and the local stress field obtained are consistent with a regional NE trending dextral transpressive shear. The relocated aftershocks show a cluster with an L-shaped pattern concentrated in a $\sim 7 \times 7$ km area. Our model defines the Algeciras fault with two structural styles for its northern termination. The NW part is characterized by a duplex-style of right-lateral strike-slip with inner secondary faults of the same sense of movement, and the SE zone by a domino-style system with inner minor faults of sinistral kinematics. The earthquake doublet is in the zone characterized by the duplex style. In contrast, the southern part of the aftershocks is located in the zone characterized by the domino style.

Plain Language Summary We studied the twin earthquakes (Mw 6.0 and 5.8) of 24 December 2019, and their sequence of aftershocks that occurred in the settlement of Mesetas, department of Meta, Colombia. The seismic activity is located 200 km south of the capital of the country in the foothills of the Eastern Cordillera in a region of high seismic potential between the Algeciras and Guaicáramo fault systems. To investigate the earthquake rupture, we used local and regional seismic waveforms to estimate seismic source properties of main events and its 17 aftershocks ($M > 4$) through several methods, such as the analysis of location, focal mechanism, finite-extent modeling of slip distribution on the assumed fault planes, and Coulomb stress transfer. Furthermore, we performed geologic and tectonic analyses, such as mapping the fault traces based on morphostructural analysis. We conclude that the Algeciras Fault System combines duplex and domino styles with dextral sense south of the Guaicáramo Fault System and defining the eastern boundary of the cordillera.

1. Introduction

Bogotá, with a population of 8 million and the capital of Colombia in NW South America, is one of the global megacities with high seismic risk (Acevedo et al., 2020; Riaño et al., 2021). A likely location of $M > 7$ earthquakes that represent a major future threat for the city is known to exist within 100 km (Algeciras Fault System [AFS], detailed below). Nevertheless, more than 50 years passed between the last M7 in this region and an Mw 6 earthquake that occurred there on 24 December 2019. The segmentation of the AFS has been the subject of discussion (Chicangana-Montón et al., 2022; Diederix et al., 2021; Velandia et al., 2005). Furthermore, despite the seismic activity recorded by the National Seismic Network of Colombia from 1993, the information on potentially tectonically active structures is still unclear. Structural details have not been defined due to lack of information and difficulty of access to the area. The studies on the 2019 Mesetas earthquake (Chicangana-Montón

Supervision: Jiří Zahradník
Validation: Esteban Poveda
Writing – original draft: Esteban Poveda, Edwin Mayorga
Writing – review & editing: Esteban Poveda, Francisco Velandia, Edwin Mayorga, František Gallovič, Jiří Zahradník

et al., 2022; Noriega-Londoño et al., 2021; Vargas et al., 2021) do not address the seismological and morphostructural analysis carried out in this work. It is the first instrumentally well-observed event and sequence in the region; thus, we integrate seismic and geological data to study the source process to contribute to the interpretation of the activated segment of the AFS. The 2019 earthquake sequence is appealing mainly because it involves two mainshocks (Mw 6 and 5.8) that occurred in a complex region close to each other in space and time (i.e., a doublet). Finally, we formulate a plausible tectonic model of the northern segment of the AFS that explains the occurrence of main events and their aftershocks.

The tectonic configuration of northwestern South America is characterized by the complex interactions of the Caribbean, Nazca, South American plates, and the Panamá-Chocó block (Figure 1a). The contact zone between these plates, known as the North Andean Block (NAB), is a tectonic unit that originated from the interaction between terranes of different affinities, ages, and stress regimes that accreted to the continental margin of NW South America (Cediel et al., 2003; Escalona & Mann, 2011; Montes et al., 2005; Spikings et al., 2015; Taboada et al., 2000). At present, the NAB moves to the northeast (Alvarado et al., 2016; Audemard & Audemard, 2002; Audemard & Castilla, 2016; Audemard et al., 2021; Diederix et al., 2021; Egbue & Kellogg, 2010; Gutscher et al., 2000; Mora-Páez et al., 2019; Nocquet et al., 2014; Trenkamp et al., 2002; Velandia et al., 2005). This movement (or escape) occurs along several fault systems that define the NAB boundary in Ecuador, Colombia, and Venezuela. Recent Global Positioning System (GPS) measurements have shown that the NAB moves at an azimuth of 60° at an average of 8.6 mm/yr relative to the South American plate (Mora-Páez et al., 2019).

The northern section of the NAB border in Colombia (north of 4°N), includes the Guaicáramo Fault System (GFS), dominated by compressive stress regimes and thrust faulting (Diederix et al., 2021; Mora & Parra, 2008), while the central part of the range is characterized by NE displacement (Mora-Páez et al., 2019) and right-lateral strike slip earthquake focal mechanisms (e.g., Dicelis et al., 2016). The southern section (south of 4°N), named the AFS, is dominated by a strike-slip and transpressive regime (Arcila, M. & Muñoz–Martín, 2019; Diederix et al., 2021; Velandia et al., 2005), see Figure 1. The latter tectonic zone has been classified as a right-lateral wrench complex geometry where geomorphology, major historical earthquakes, and recent seismic events indicate neotectonic activity (Chicangana-Montón et al., 2022; Diederix et al., 2021; Noriega-Londoño et al., 2021; Velandia et al., 2005). The most recent paleoseismology study (Diederix et al., 2021) reports that at least seven $M > 7$ events have occurred along the AFS since 8,120 ± 145 BCE at the Algeciras pull-apart basin.

The AFS is one of the most seismically active and continuous fault systems in Colombia and has produced the largest historical crustal earthquakes in the country, with estimated magnitudes, at these historical times: M6+ on February 1616, M7+ on 6 March 1644 and 18 October 1743, Mw 7.1 on 12 July 1785, and Mw 6.7 on 31 August 1917 (Cifuentes & Sarabia, 2009). The last Mw 7.0 earthquake on 9 February 1967 destroyed some populated areas and even affected Bogotá, resulting in hundreds of deaths and extensive damage (Cifuentes & Sarabia, 2009; Dimaté et al., 2005). An Mw 5.9 earthquake on 24 May 2008, occurred close to the GFS (Dicelis et al., 2016), see Figure 1.

From a regional point of view, the transition between the AFS and the GFS is proposed as connected systems (Taboada et al., 2000; Velandia et al., 2005); although other authors also proposed that the GFS is not directly connected with the AFS. The right lateral dextral displacement of the NAB only began about 2 Ma (Egbue & Kellogg, 2010). This displacement to the NE is transferred from the AFS to a wide zone of dextral faulting in the Eastern Cordillera as evidenced by GPS measurements and earthquakes (Dicelis et al., 2016; Mora-Páez et al., 2019). To characterize the Mesetas earthquake sequence related to AFS, we mapped the fault traces based on hillshade images from digital elevation models with 30 and 12.5 m resolution (NASA—Alaska Satellite Facility) (https://vertex.daac.asf.alaska.edu). From identifying morphostructural structures related to main and secondary faults, we highlighted the northern termination of the AFS before its junction with the GFS since the whole system consists of several regional faults with significantly related earthquakes (Figure 1). This information was used with seismological observations to identify new related structures and interpret the Mesetas seismic sequence.

On 24 December 2019, an earthquake sequence started with two almost identical major earthquakes (Mw = 6.0 and Mw = 5.8) near the Mesetas settlement in the Eastern foothills of Colombia, approximately 200 km southeast of Bogotá (Figures 1 and 2). The two events occurred just a few kilometers and 16 min apart, forming a doublet. They were preliminarily located by the National Seismic Network (https://www.sgc.gov.co/sismos) at 3.453°N and 74.194°W and 9 km in depth and 3.474°N and 74.242°W and 12 km in depth, respectively. Some

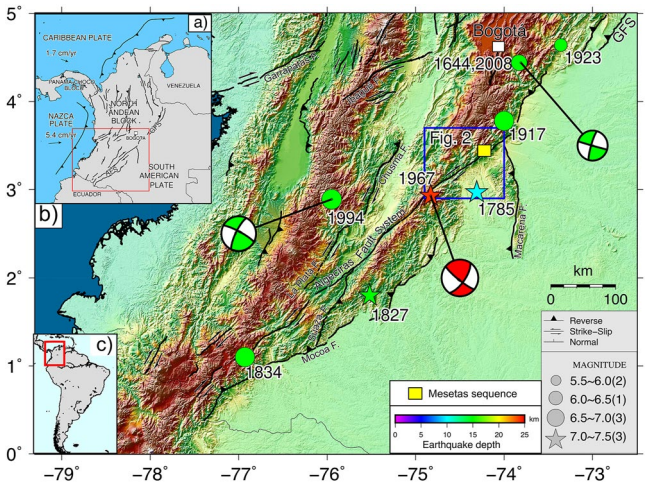

Figure 1. (a) Simplified tectonic framework of NW South America with main tectonic structures (Nazca, Caribbean, South America and North Andean Block), Guaicáramo Fault System, and Algeciras Fault System (AFS) from the Global Active Database (Styron & Pagani, 2020). The vectors show the Global Positioning System-derived motion of the Nazca and Caribbean plates relative to the South American plate (Mora-Páez et al., 2019). (b) Historical seismicity in SW Colombia, color-coded by earthquake depth, with focal mechanisms from the Global Centroid Moment Tensor catalog and Mw 7.0 on 9 February 1967 from Suárez et al. (1983). Major earthquakes (1785, 1827, 1834, 1967, and 1917) are related to the AFS. Other important faults are also shown (Styron & Pagani, 2020; Veloza et al., 2012). The blue square represents the location of Figure 2, the principal area of this study. (c) The red rectangle shows the location of (a).

damage to weak buildings was reported, most of which included cracks in cladding, cracks in walls, roof tiles falling, and cracks in structural joints between columns and beams. The following seismic sequence of about 412 aftershocks of $M > 2.0$ lasted 3 months and showed an L-shaped pattern, suggesting complex faulting (Figure 3a). The seismic sequence was situated less than 100 km northeast of the 1967 Mw 7.0 earthquake in the junction between the GFS and the AFS with a complex fault network. Therefore, the 2019 Mesetas sequence is essential in terms of magnitude and consequences. The present study reveals newly identified structures in the current complex boundary of the Northern Andes.

The Mesetas sequence was well recorded by broadband and strong-motion seismic networks, providing a unique opportunity to decipher the rupture processes and contribute to the knowledge of the fault segments of the AFS. We model the largest events in terms of centroid moment tensors, space-time development of slip on the faults, local stress field, and Coulomb stress transfer. Seismology and geology results are combined to improve understanding of the complex faulting style of the Algeciras Fault. We interpret the mainshocks and the aftershocks as related to the activity of the northern termination of the AFS, where two structural styles control the seismic activity, as we show later. These results reveal unprecedented details about newly identified active faulting in this complex yet poorly known region.

2. Tectonic Setting

The study area occupies the eastern boundary of the NAB (Figure 1a), which is referred to by some authors as the Eastern Front Fault System (EFFS) in Colombia and Venezuela (Audemard & Audemard, 2002; Audemard et al., 2021; Diederix et al., 2020; Kellogg et al., 1995; Pennington, 1981; Taboada et al., 2000). In Colombia the EEFS is outlined by the GFS, while the AFS crosscuts the Eastern Cordillera and the whole Andes since connecting with the Chingual-Cosanga-Pallatanga-Puna fault system up to the Gulf of Guayaquil in Ecuador, defining the eastern tectonic boundary of the NAB (Alvarado et al., 2016; Velandia et al., 2005).

The Eastern Cordillera border is interpreted as the result of transpression generated by right lateral movement of the AFS and the EFFS during the Quaternary (Audemard & Audemard, 2002; Audemard & Castilla, 2016; Diederix et al., 2021; Gutscher et al., 2000; Mora-Páez et al., 2019; Nocquet et al., 2014; Trenkamp et al., 2002), promoting the "escape" of the Northern Andes to the NE with respect to the South American Plate. The motion along the AFS is predominantly dextral strike-slip type with a reverse component (Chicangana-Montón et al., 2022; Noriega-Londoño et al., 2021; Velandia et al., 2005). Between 4°N and 7°N, the GPS results show primarily dextral strike-slip in the Eastern Cordillera (Mora-Páez et al., 2019). However, other pieces of evidence from focal mechanisms (Garcia-Delgado et al., 2022) show local values of SHmax with orientations perpendicular to GFS between 5°N and 6°N. The geomorphic expression of AFS is characterized by several pull-apart, rhomboidal shaped, and releasing sidestep basins (Diederix et al., 2021; Velandia et al., 2005). Furthermore, synthetic and antithetic faults and folds oriented obliquely to the main trace of the system are observed (Diederix et al., 2020, 2021; Velandia et al., 2005). The AFS behaves like a right lateral structure, with a vertical component in which sedimentary cover and basement rocks are involved (Velandia et al., 2005).

The continuity of the AFS to the north was interpreted as connecting the GFS along the eastern piedmont of the Eastern Cordillera (Velandia et al., 2005), but also trending NE along the Río Meta Fault (Audemard & Castilla, 2016; ; Mora et al., 2013). Nevertheless, here, we constrain the northern termination of the AFS as a regional and independent structure with its own style.

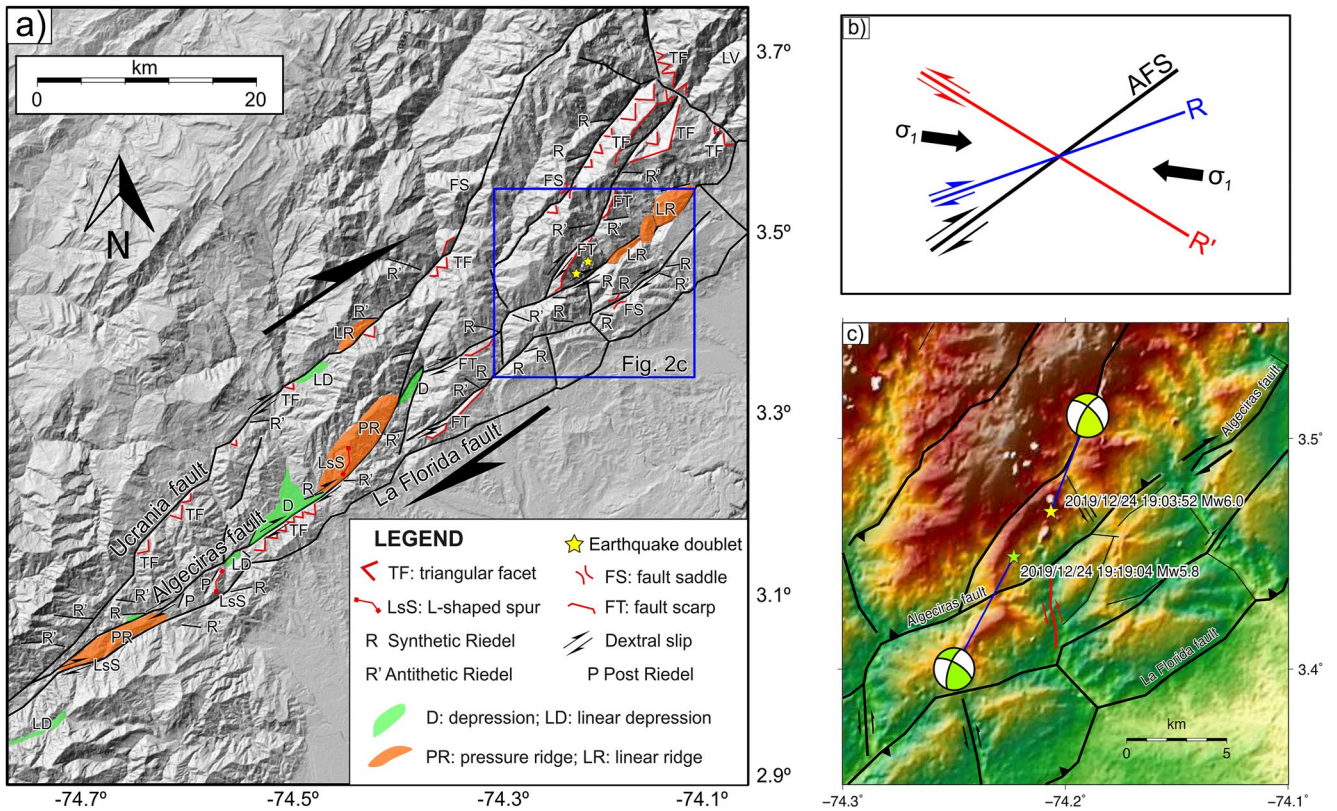

Figure 2. (a) Map with detailed morphostructural features interpreted along the Algeciras fault system. The blue square represents the zone of (c). (b) Schematic showing the relationship between major transpressional shear zone of Algeciras Fault System, the Riedel traces and the orientation of σ_1 based on Woodcock and Schubert (1994). (c) Location of earthquake doublet that occurred on 24 December 2019, with detailed fault mapping and focal mechanisms obtained in this study. The segment in red represents one of the identified structures, which will be discussed later in relation to seismicity.

3. Morphostructural Mapping

Since it is necessary to obtain details of the geological faults, we supplement existing regional geology information with our analysis to constrain the Mesetas seismicity and its relationship with the structural framework. In particular, we developed the morphostructural mapping of the AFS (Figure 2a). Within the geomorphic structures, we identified pressure and linear ridges proper of restraining bends and contractional oversteps, as well as some linear depressions that are located along releasing bends of the main fault system. Other geological features can be observed, such as triangular facets, fault scarps, L-shaped spurs, fault saddles, offset and drainage control (Figure 2a), all of them as signs of neotectonic activity and located according to dextral strike-slip kinematics. Although, the configuration of the structures (e.g., orientation) can be affected by previous fracture patterns of the geological massif, dextral kinematics of the whole system is confirmed by the geometry and orientation of the splay of secondary faults (Riedel traces): ENE (R or synthetic fault), E (R' or antithetic fault), and NNE (P or post-synthetic fault), while the AFS is trending NE (Figure 2). These synthetic and conjugate faults work on drainage organization and the configuration of some ridges and depressions.

The complete set of the main geological faults (Ucrania, Algeciras, La Florida—Figure 2a), subparallel between them, as well as the location and orientation of morphostructures and related minor faults, are considered evidence to propose a local stress tensor that explains the kinematics, and two structural styles of the fault damage zone. Following Woodcock and Schubert (1994), the general fault array and the associated minor faults result in a stress tensor orientation with σ_1 in azimuth of 100° (Figure 2b), which supports dextral strike-slip of the AFS in the area. The morphostructural style shows the thickening of this fault system toward the north, defining its termination along a regional restraining bend. The fault geometry of this transpressional termination can be explained by two domains from the main trace of the Algeciras fault (Figures 1 and 2): duplex and domino styles (in plan view),

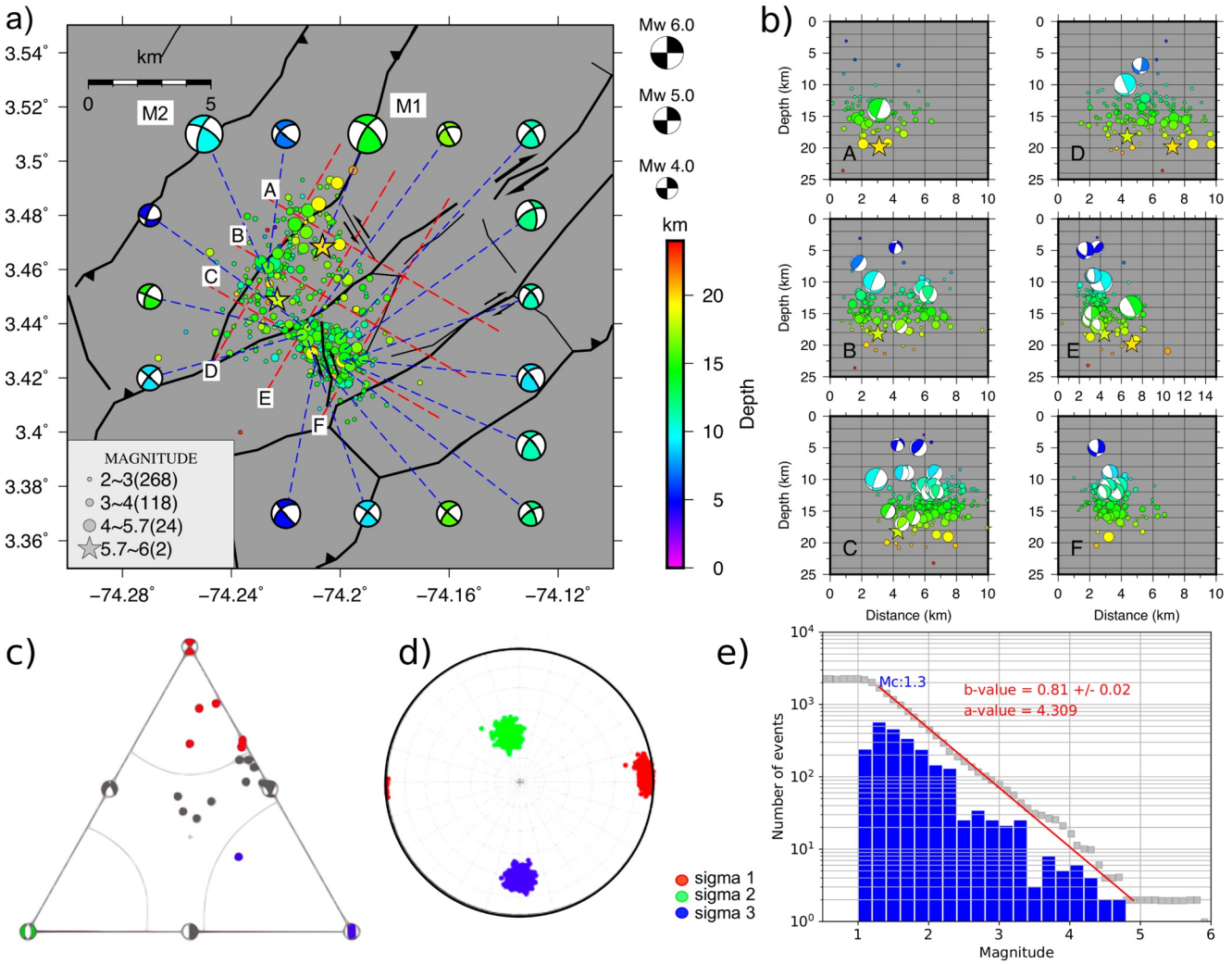

Figure 3. (a) The Mesetas doublet (yellow stars) and aftershocks Mw > 2, color-coded by earthquake depth. The event symbols and focal mechanisms are scaled by magnitude. Focal mechanisms are depicted for the aftershocks of Mw > 4. (b) Selected vertical sections based on the seismicity L-pattern and strike of M1 and M2, along profiles of Panel (a) Shown in the sections are the events situated within a 1.5 km wide band. (c) Ternary diagram obtained from focal mechanisms. (d) Principal stress axes derived from the studied sequence based on the StressInverse code (Vavryčuk, 2014). (e) Magnitude-frequency distribution and Gutenberg-Richter law for Mesetas sequence. Blue bars represent the number of earthquakes inside each 0.2 magnitude interval. The red straight line represents the Gutenberg-Richter law obtained by fitting the cumulative events (squares) using a maximum curvature solution (Wiemer, 2001).

detailed in the discussion section. Additionally, as a result of the mapping, a structure is highlighted (Figure 2c, in red) related to seismicity, which will be addressed later.

4. Relocation of the Mesetas Sequence

The Mesetas earthquake sequence comprised 412 events of $M > 2$ (Figure 3). The first arrivals of P- and S-waves were manually picked using 64 stations (Figure 4). The locations were first determined with the NonLinLoc code (Lomax et al., 2000) in the velocity model of Pedraza and Pulido (2018); this model agrees with a previous study of receiver functions and ambient noise tomography (Poveda et al., 2018) developed in the zone. The NonLinLoc locations provide quite a diffuse foci distribution (Figure S4 in Supporting Information S1). We then relocated the sequence using the HypoDD code (Waldhauser & Ellsworth, 2000) with the same velocity model, and the foci were efficiently clustered (Figure 3) with horizontal errors below 30 m and less than 40 m in depth. We used HypoDD for earthquakes above magnitude 2 recorded at least by 9 seismic stations; we do not use waveform cross-correlation. The epicenters indicate an L-shaped pattern (Figure 3a). It formed within a few hours after the mainshock and remained stable for the whole ~160-day duration of the sequence (Figures S2

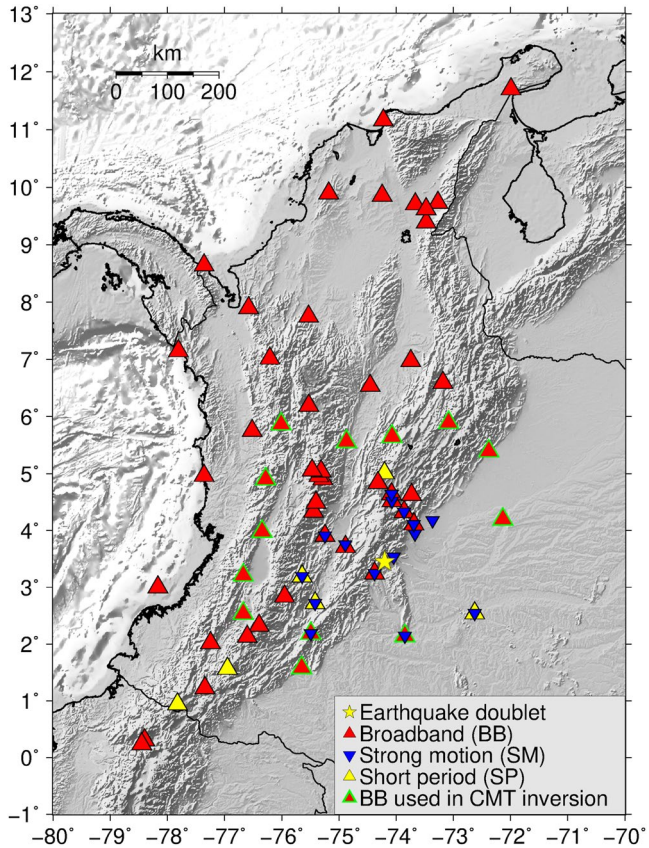

Figure 4. Seismographs used in this study. Stations of the Servicio Geológico Colombiano were supplemented by two stations of neighboring countries (see also Table S1 in Supporting Information S1). Broadband (red triangles), short period (yellow triangles), and strong-motion (blue inverted triangles) stations were used to locate mainshocks M1 and M2 and aftershocks. For kinematic slip inversion, we used only the near-source strong motion network, whereas, for Centroid moment tensor inversion, we used a combination of broadband stations (red triangles with green borders) and the strong motion network.

and S3 in Supporting Information S1 with 24 hr and 160 days, respectively). The sequence occurred between depths of 5 and 20 km in a 7 × 7 km area (Figure 3). The frequency-magnitude relationship of the sequence was studied by calculating the Gutenberg-Richter relation with the maximum curvature method and ZMAP code (Wiemer, 2001). The obtained *b*-value = 0.81 is relatively low (Figure 3e), in agreement with Frohlich & Davis, 1993 related to the multiple-fault Algeciras System in a transpressive environment.

For the two mainshocks, M1 and M2 (Mw 6.0 and 5.8, respectively), a detailed uncertainty analysis of their hypocenter position was performed, as shown in Figure S5 in Supporting Information S1. We used the Oct-Tree method implemented in NonLinLoc, which samples the location probability density function ("scatter cloud"). Due to the network geometry and picking errors, the clouds are elongated approximately in the N-S direction. Dimensions of the M1 cloud based on its confidence ellipsoid are 7.7 km for the major axis and 2.2 km for the intermediate axis. Likewise, for M2, we found values of 7.9 and 1.6 km for the major axis and intermediate axis, respectively. The RMS location errors for the M1 and M2 events are 0.34 and 0.31 s, respectively.

Two mainshock locations are shown in Figure 3a. Their hypocenters are situated at a depth of 18–20 km (Figure 2b). Within the uncertainty, the epicenter of M2 is shifted ∼2 km in the southwestward direction relative to M1. Although the best-fit hypocenter of M2 is ∼5 km shallower than M1, their relative depth shift is less well resolved (see Figure S5 in Supporting Information S1 which also shows a trade-off between depth and the NS position).

5. Moment Tensor Solutions

Centroid moment tensors (CMTs) were determined by full-waveform inversion of 29 near-regional records, 14 broadband, and 15 strong-motion stations (code ISOLA, Zahradník & Sokos, 2018). Records from broadband and strong motion stations were used (see Figure 4), comprising epicentral distances between 31 and 335 km and relatively low frequencies (0.02–0.05 Hz). The selection of stations and frequency bands was based on the data quality, requiring low noise and the absence of instrumental disturbances. Moment tensor was obtained by the least-squares method, assuming a single-point source model. Centroid depth was grid searched beneath the epicenter of each event. Green's functions were calculated with the same 1D model as used for the locations (Pedraza & Pulido, 2018; Figure S1 in Supporting Information S1). The depth variation of the correlation between real and synthetic seismograms for the mainshocks is shown in Figure 5, and the respective waveform fit is displayed in Figure 6.

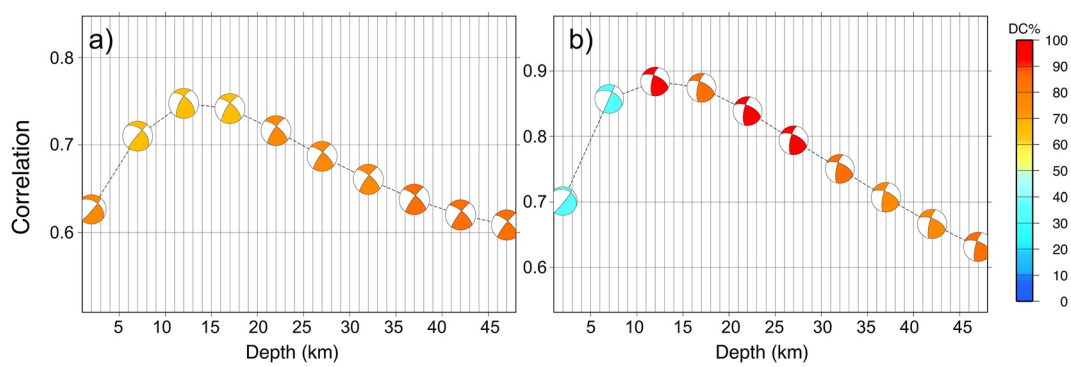

Figure 5. Depth variation of the single point-source deviatoric MT model of the (a) M1 and (b) M2 mainshocks.

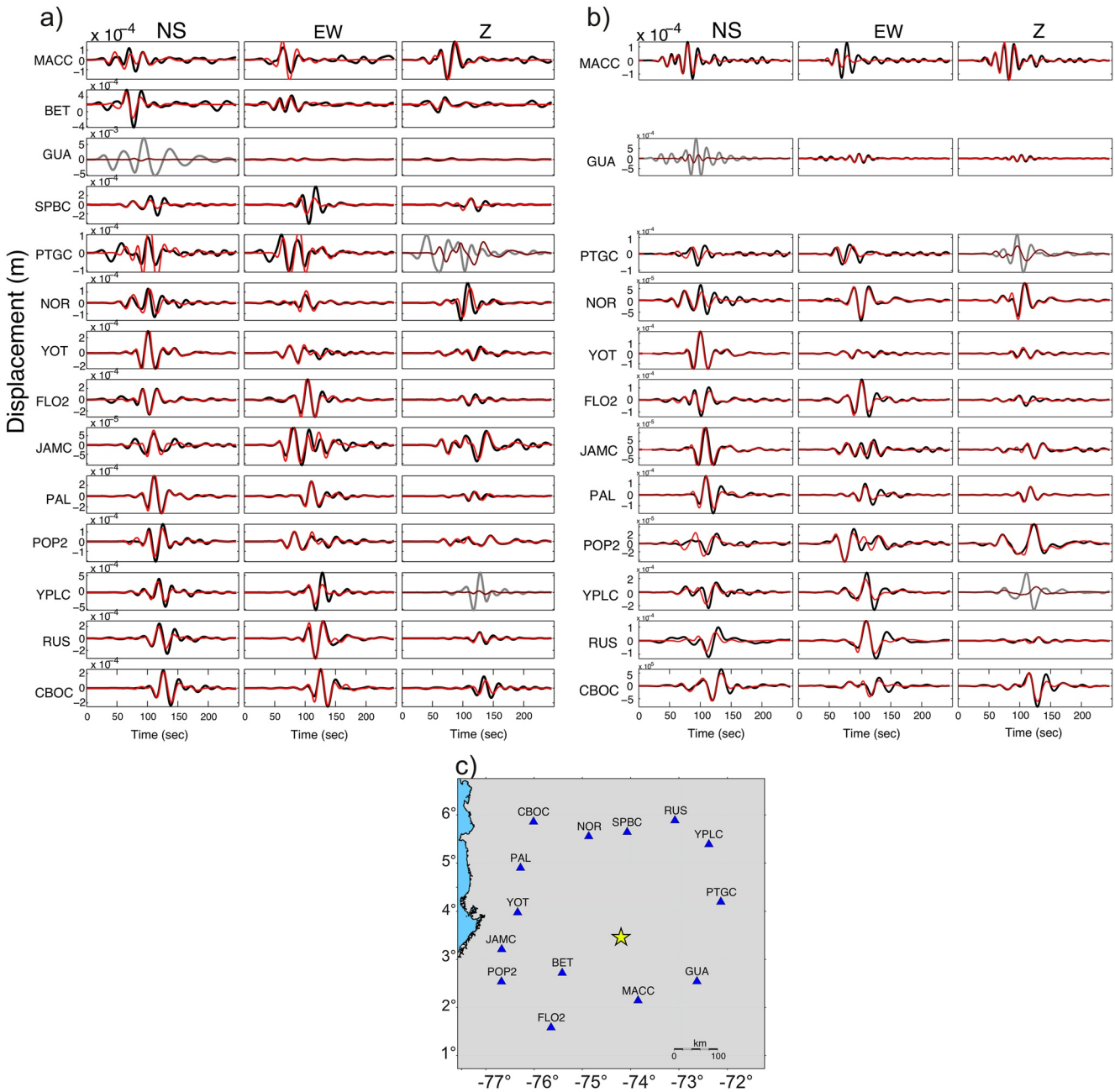

Figure 6. The fit of the observed (black) and synthetic (red) displacement waveforms (in meters) for the single point-source deviatoric-MT model of the (a) M1 and (b) M2 mainshocks. Stations are sorted by epicentral distance from 150 to 334 km. Both data and synthetics are bandpass Butterworth filtered between 0.02 and 0.05 Hz. The components with bad fit (gray) were removed from the inversion. (c) Seismic stations of the Servicio Geológico Colombiano used in the inversion. The stations BET and SPBC were not used in the M2 inversion due to instrumental disturbances in the records.

Interestingly, the moment tensor solutions of M1 and M2 are almost identical, featuring a strike-slip mechanism with a reverse component, characterized by strike/dip/rake (s/d/r) angles 210°/73°/158° and 197°/72°/156° for M1 and M2, respectively. The M1 and M2 events were observed by international networks. The Global Centroid Moment Tensor (Global CMT) project (Dziewonski et al., 1981; Ekström et al., 2021) estimated a centroid depth of 19.2 km with strike/dip/rake (s/d/r) 208°/67°/154° angles for M1, and a centroid depth of 18.2 km with a fault plane of 195°/69°/158° for M2, respectively. We did not have a prior preference for rupture of these or conjugated nodal planes. The centroids are situated at depths of 10–14 km, and the double-couple percentage of M1 (<80%, Figure 5) is lower than that of M2 (>80%). The CMT inversion is stable around the best-fitting depth, and the

waveform fit between real and synthetic seismograms is very good, with variance reduction VR ~ 0.87 and ~0.86 for M1 and M2, respectively (Figure 6). For details, see Table S2 in Supporting Information S1. CMTs of 14 aftershocks (Mw > 4) exhibit a mix of strike-slip and reverse faulting, and centroid depths ranging between 5 and 17 km (Figure 3). We used the 29 focal mechanisms solutions (Figure 3) from moment tensor inversion to apply the StressInverse code of Vavryčuk (2014), characterize the compressive stress orientations, and evaluate the possible relations with mapped faults. The results are shown in Figure 3d and addressed in the discussion section.

6. Inference About Faults and Their Seismic Slip

In this section, we present plausible kinematic models of the two mainshocks (Figure 7). The space-time distribution of the slip and slip rate is calculated by linear full-waveform inversion using the LinSlipInv method (LSI, Gallovič et al., 2015), developed and thoroughly tested in recent years (Gallovič, 2015; Mai et al., 2016; Pizzi et al., 2017). Model parameters are samples of the slip-rate time function over a gridded fault and over the whole duration of the source process. The inversion is regularized by smoothing, by ensuring slip-rate positivity, and by seismic moment (estimated in the CMT inversion). Optimal free parameters of the slip inversion were established by extensive testing: (a) subfaults are 1 × 1 km, (b) frequency range of 0.05–0.20 Hz for all stations of Figure 8, (c) smoothing between 0.01 and 0.05 m, which represents the data error in the method. Some stations or components were effectively removed from the inversion by down-weighting by a factor of 0.001; the station components remained in the modeling to check how they were predicted by the slip model derived from the remaining stations (shown in gray in Figure 8 and Figure S6 in Supporting Information S1 with a bad fit between real and simulated seismograms). In this method, the rupture model is inverted without prior constraints on the position of the nucleation point. The inversion of each event requires a predefined fault plane. To constrain the likely fault planes, we examine and combine several pieces of information, such as the position of hypocenters, centroids, aftershocks, as follows.

Beyond the L-shaped aftershock distribution seen in the map view of Figure 3a, in 3D, it is not easy to recognize simple geometrical structures, such as possible fault planes, because (as indicated above by the focal mechanisms) the involved faults are not vertical. Another issue is that aftershocks, although relatively well clustered by double-difference relocation, are still dispersed, partly due to the possible activation of several different short faults. In this study, we construct approximately 100 trial faults of the two mainshocks as planes passing through their hypocenters. Both nodal planes of all trial faults are tested as potential fault planes in the slip inversion. To select the best fault planes, several model comparison techniques were proposed, such as cross-validation (e.g., Wahba & Craven, 1978) and the evidence ratios (e.g., Sambridge et al., 2006; Yañez-Cuadra et al., 2022), for instance. In this study, we select the best fault planes based on the principle of Occam's razor (e.g., Constable et al., 1987). We seek for good stability and quality of the parameters in the inversion, without overfitting the data, as well as looking for fault planes located and oriented in agreement with the seismicity spatial distribution and morphostructural observations. We note that we do not account for epistemic errors caused by uncertain fault definition (e.g., Ragon et al., 2018). Although the latter technique is available for simplified cases, it is unclear of how to implement it within the comparison of our fault definition with seismicity and morphostructural observations.

Based on the CMT (s/d/r angles) and the aforementioned tests, we suggest two scenarios, A and B (see Figure 7). In both scenarios, mainshock M1 has a fault plane striking at 210° and dipping 70°. The conjugate nodal plane of M1 was denied for its poor waveform fit in the kinematic slip inversion (Figure S6 in Supporting Information S1). Regarding M2 (motivated by the L-shaped aftershock pattern), in scenario A, this event is assumed to have ruptured in the second nodal plane characterized by a strike of 298° and dip of 60°. In scenario B, the M1 and M2 fault planes are almost parallel, with M2 characterized by a strike of 197° and dip of 70°.

Slip models are shown in Figure 7a. We note that they are heavily smoothed due to the stabilizing constraint; that is why the models resemble rather a smoothed centroid, which could be improved only if (more) local stations were available. Stable and unstable features of the slip rate and slip distributions can be identified in Figures 7b and 7c, respectively. We set time $t = 0$ at 3 s before the origin time of M1 and at 2 s before M2. The stable features are as follows: (a) M1 consists of the main moment release at $t = 4$ s, continuing for the next 2 s ($t = 5$ and 6 s) with a still significant slip rate. The estimated slip rate of M1 agrees with the SCARDEC source time function database (Vallée & Douet, 2016), whose results has a maximum rate of 4 s and a duration of 6 s (b) M2 is simpler

10.1029/2022EA002465

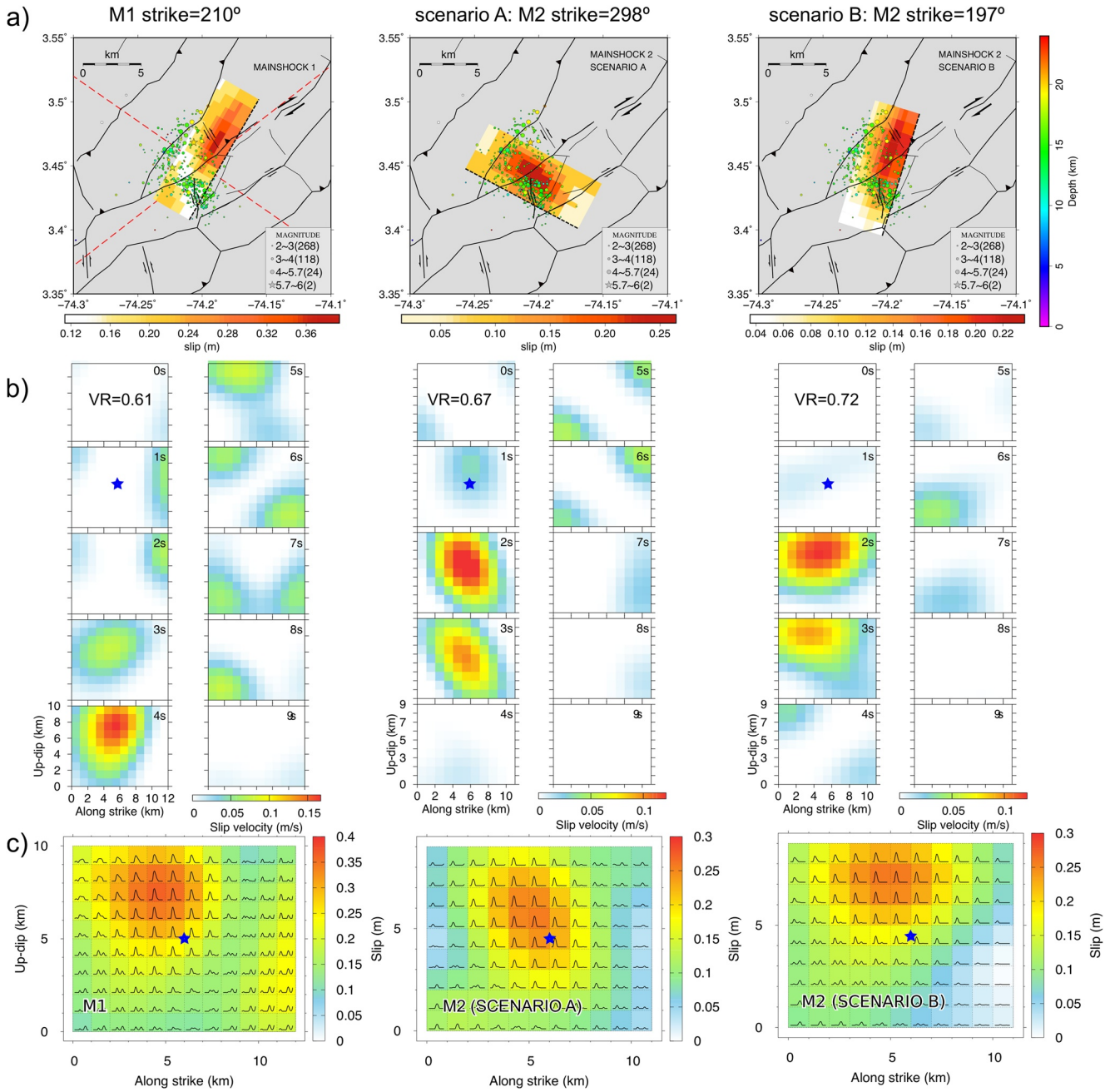

Figure 7. (a) Proposed scenarios A and B of the two mainshocks. The M1 fault plane is fixed, while two trial positions of the M2 plane are considered. The top edge of the fault is marked by the thick line. Superimposed on M1 are the optimally oriented faults of the region (dashed lines). (b) Space-time evolution of the slip rate. Left column—M1, middle and right columns—M2 in scenarios A and B, respectively. The snapshots are marked with time, 0–9 s; $t = 0$ is 3 and 2 s before the respective origin time of M1 and M2, respectively. Variance reduction marks variance reduction of the waveform inversion. (c) Final slip distribution, arranged similarly to Panel (b) Note the different scales of the subpanels. The blue stars are hypocenters from the NonLinLoc location (not used as a constraint for the rupture nucleation position) at depths of 12 and 15 km for M1 and M2, respectively. In each subfault the source time function is displayed.

due to its smaller magnitude, primarily rupturing at $t = 2$ and 3 s. Less stable features include disturbances, or "ghosts" (i.e., regions of low slip rate), for example, at $t = 2$ s in M1 and $t = 5$ and 6 s in M2. The ghosts are artifacts common to all slip inversions due to imperfect modeling, such as an inaccurate position of the fault or an inaccurate velocity model (Gallovič & Zahradník, 2011; Gallovič et al., 2015; Zahradník & Gallovič, 2010). In our case, M2 with a strike of 197° (scenario B) provides a cleaner slip-rate pattern in the initial phase of the process ($t = 0$ and 1 s), and the waveform fit (VR) is higher than that of scenario A. The waveform fit of scenario

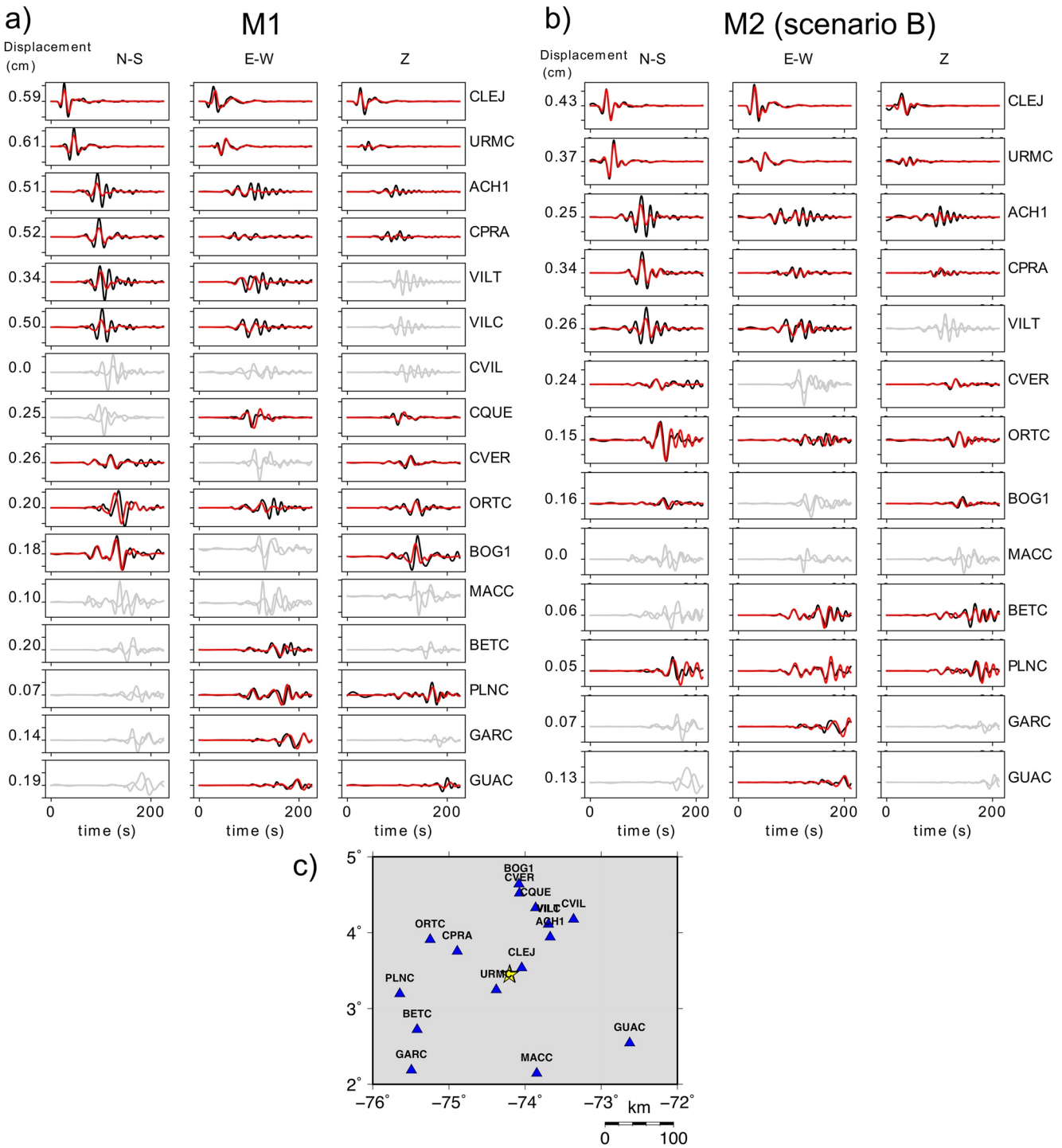

Figure 8. Comparison between observed (black) and simulated (red) waveforms for (a) mainshocks M1 and (b) M2 in scenario (b) The gray traces represent the components with poor fitting, unused in the inversion. The station codes are on the right. Peak observed displacements are shown to the left. (c) Strong motion stations of the Servicio Geológico Colombiano used in the slip inversion.

A is worse, especially for near stations (Figure S6 in Supporting Information S1). Scenario B fits seismic data in the 0.02–0.5 Hz range with variance reduction (VRs) of 0.61 for M1 and 0.72 for M2 (see Figure 8). For these reasons, we prefer scenario B, that is, M1 (strike 210°) together with M2 (strike 197°). Furthermore, we discuss which of the scenarios should be preferred in the Discussion section, considering additional arguments.

We do not broadly discuss the absolute size of the slip patches (10 × 10 km) and the maximum slip (~30–40 cm) for two reasons: they are not critical from the tectonic viewpoint, and they depend on the adopted smoothing. We tested suitable spatial smoothing following Gallovič et al. (2015). The smoothing parameter of 0.01–0.05 m was chosen as a compromise between the simplicity of the slip pattern (minimum "ghost" features) and the waveform data fit. Nevertheless, our slip model agrees with empirical relations (Somerville et al., 1999; Wells & Coppersmith., 1994) that predict 30 and 16 cm of maximum slip for M1 and M2, respectively. Regarding the space-time development of M1 and M2, we find in Figures 7b–7c that rupture propagated basically upward. In M1 and M2 (scenario B), we also detected an anti-strike component of rupture propagation in the north-northeastward direction (i.e., at a 20° azimuth).

7. Discussion

The geomorphological features of AFS are consistent with a transpressional system with secondary faults and local restraining bends of the oblique structures. This setting is similar to some global examples (Mann, 2007) and is defined as a positive flower structure. We propose that the whole fault set, well expressed by the geological and geomorphological evidence, defines two structural styles (Figure 10), characteristic of strike-slip kinematics: (a) a dextral transpressive duplex, with the Ucrania fault as the northwestern border, where the inner faults are oblique and subparallel to the shear faults and resolve with the same dextral strike-slip kinematics, and (b) a recent domino-style system, where La Florida fault constitutes the southeastern frontal trace of a positive flower structure, as a shortcut from the Algeciras main fault; and among these main structures, a set of inner secondary faults show opposite kinematics (sinistral). These minor domino faults cross by a longitudinal back-thrust fault verging northwest, implying the internal rotation of the minor blocks (Figure 10b). As examples, several mixed tip damage zones at the terminations of strike-slip faults are explained by Kim et al. (2004), including a comparable case between the San Andreas and San Jacinto faults in California.

As inferred from the previous analysis, the fault interpretation of M1 mainshock is well constrained, while M2 is unclear. Therefore, we discuss the two scenarios from the viewpoint of aftershock locations, Coulomb stress transfer, and tectonic interpretation.

Regarding the aftershock distribution relative to the fault planes, there is no significant preference for scenarios A or B. This can be seen in Figure S8 in Supporting Information S1 and even better if using our 3D plotting tool (GUI_Mesetas), included in Supporting Information S1 of this paper. Indeed, the aftershock cloud seen in the map view as the SE trending arm of the L-shaped pattern (Figure 3a) can be explained by M2 with a strike of 197° (scenario B), not strongly requiring a strike of ~298°, orthogonal to M1. If M2 ruptured the plane striking at 298° according to scenario A, many aftershocks project onto the main slip region of that event, unlike M1 (Figure 7a). In scenario B, both M1 and M2 events have their major slip regions associated with the paucity of aftershocks, similar to many other earthquakes (e.g., Das & Henry, 2003; van der Elst & Shaw, 2015; Wetzler et al., 2018). Thus, we consider the aftershocks to support scenario B. The interpretation of the seismological data presented above is well constrained and related to the transpressive structure of the AFS, whether to the duplex of the NW domain or the transverse faults of the SE domino (in plane view). As indicated in Figure 7a, the subparallel faults of M1 and M2 (scenario B), both characterized by right-lateral strike-slip motion with a reverse component, fit well into the general framework of the left-stepping restraining bend.

The estimation of the stress field using the StressInverse code by Vavryčuk (2014) is shown in Figure 3d. It is characterized by the principal stress axes σ_1 azimuth/plunge = 88°/4°, σ_2 = 350°/61°, σ_3 = 180°/29°, and a stress-shape ratio of 0.56. This stress field has two optimally oriented faults (OOFs), characterized by s/d/r (°) = 232/63/168 and 305/69/21 (see Figure 7a). In this context, we can speculate that each mainshock ruptured one of these two OOFs. Such examples have been documented in the literature (e.g., Fojtíková & Vavryčuk, 2018; Noisagool et al., 2016; Singh et al., 2017; Vavryčuk, 2011) and would favor scenario A. Nevertheless, scenario B also remains plausible, that is, stress-favored, with both M1 and M2 rupturing close to one of the OOFs (within 30° in terms of Kagan angle) with the reactivation of a minor transversal fault of the domino domain, according to the SE side of the L-shaped aftershock pattern.

Note that the transpressive regime (with parallel faults such as in scenario B) is supported by the focal mechanisms of aftershocks (see the ternary diagram in Figure 3c) as noted also by Noriega-Londoño et al. (2021). Furthermore, the tectonic escape of the NAB northeastward that takes place along the AFS and GFS, was suggested by

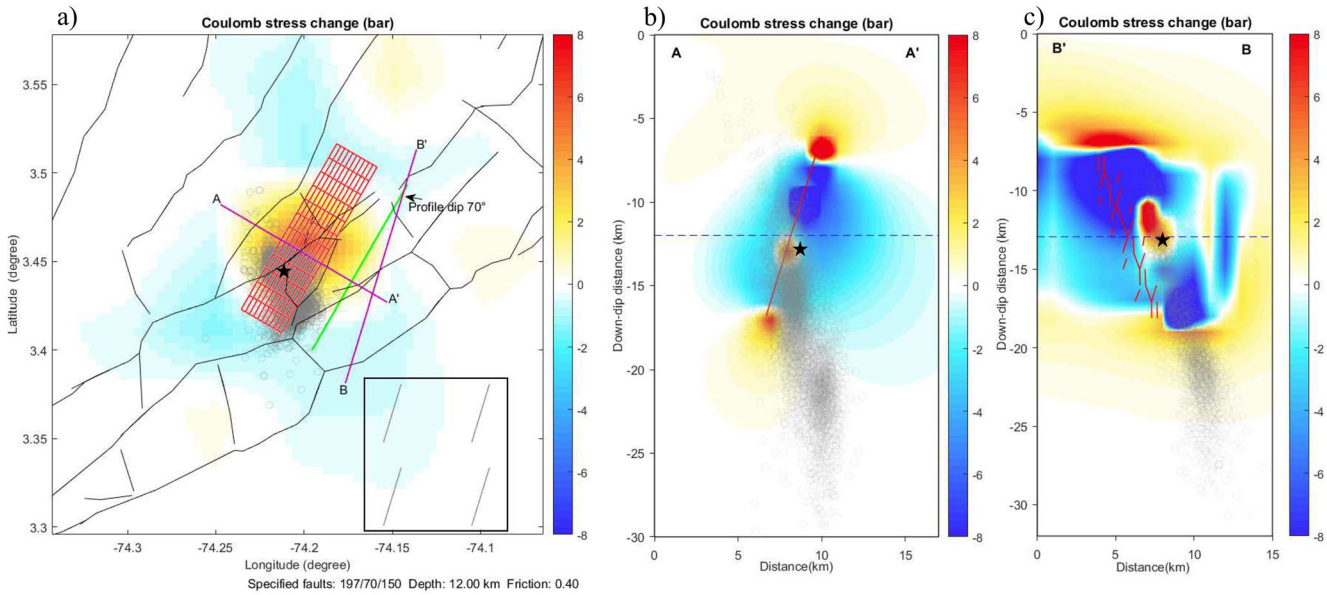

Figure 9. (a) Coulomb stress transfer for scenario B with the M1 generating fault (213°/73°/158°) and M2 receiving fault (197°/70°/150°). The stress is plotted for a depth of 12 km, the segmented lines on the map show the strike of the receiver faults, and the red grid represents M1. The gray points represent the uncertainty of the absolute location of M2 from NonLinLoc, the star is the best-fit location of M2, lines A and B represent profiles, and the green line represents the projection of the fault top edge of M1 on the surface. (b) Profile A with a vertical dip (90°) and (c) Profile B with a 70° dip as M2. The red line represents a segment of the rupture area of M1, and the dashed blue line is the assumed M1 fault-center depth. Note the stress concentration on B-B' close to the star at a depth of 12 km, supporting scenario (b).

several authors (Alvarado et al., 2016; Audemard & Audemard, 2002; Diederix et al., 2021; Gutscher et al., 2000; Kellogg et al., 2019; Nocquet et al., 2014; Trenkamp et al., 2002; Velandia et al., 2005) and confirmed by Mora-Páez et al. (2019) who estimated a velocity of 8.6 mm/yr. This movement direction also favors scenario B (according to the main fault system). This escape rate in the Eastern Cordillera is greater than the rate of range-normal shortening (4.3 mm/yr; Kellogg et al., 2019).

Owing to the spatial and temporal proximity of the mainshock, it is possible to assume that M2 was triggered by static Coulomb stress transfer from M1. The Coulomb 3.3 software (Toda et al., 2011) was used. We applied the slip distribution of M1 (Figure 7c) and calculated Coulomb stress transfer to receiver faults everywhere in space with focal mechanisms of M2 in scenarios A and B. The effective coefficient of friction was 0.4; this is a moderate value typically used for strike-slip or unknown faults (Parsons et al., 1999; Toda et al., 2011). We investigated whether a positive change correlates with the hypocenter position of the M2 mainshock, including its uncertainty documented in Figure S5 in Supporting Information S1. Figure 9 and Figure S7 in Supporting Information S1 show the Coulomb stresses for the two receiver focal mechanisms. Positive stress zones were compared with the hypocenter of M2, considering its NonLinLoc uncertainty (Figure S5 in Supporting Information S1). We found that, in general, stress transfer supports M2 situated near the lower and southwestern edges of the M1 rupture region, but neither scenario A or scenario B could be strongly preferred due to uncertainty in the M2 depth (Figure 9 and Figure S7 in Supporting Information S1). However, if considering the best-fitting NonLinLoc location of M2, scenario B is preferred, since the M2 depth would correlate with significant positive stress concentration (right panel of Figure 9).

The AFS (before its junction with the GFS) shows dextral transpressional kinematics, through a positive flower structure, which shows combined structural styles: duplex and domino (Figure 10). The Mesetas doublet and its aftershocks occurred in this zone, where these styles are separated by AFS. The aftershocks locations from NLL, HypoDD, and the CMT inversion suggest that M1 and M2 (scenario B), ruptured within AFS close to duplex style, consistent with dextral and transpressive kinematic. The formed L-shaped seismicity is located between both styles, the northern section of *L* is located on duplex style, and the southern part in the domino style, which matches with an inner secondary fault with opposite kinematics (Figures 2c and 10c, in red). Our results suggest the activity of this identified fault, which has an approximate length of 3.5 km according to geological mapping (Figure 2). Considering the rupture of M2 (scenario A) within this fault, it would not be possible to produce an

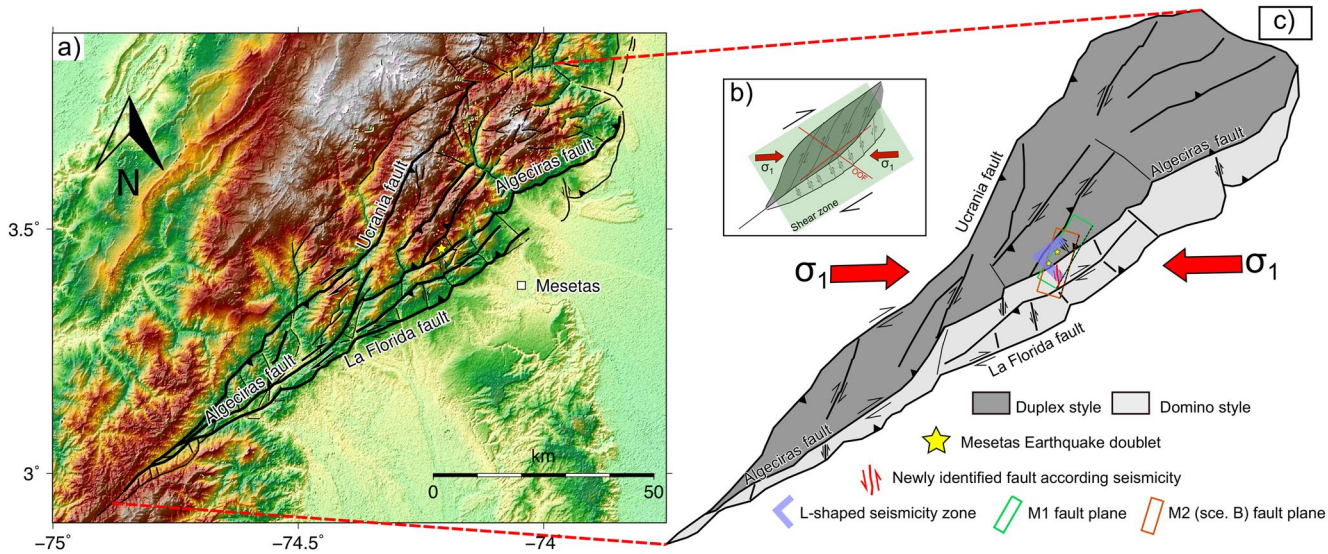

Figure 10. (a) General view of northern termination of the Algeciras Fault System (AFS) with the major central fault and the Ucrania and La Florida as the borders of the transpressive system (positive flower structure). (b) Schematic illustration to explain the mixed style of the termination of the AFS, and the optimally oriented faults from stress analysis. (c) Sketch of the northern termination of the AFS as a restraining bend zone, including the duplex and domino styles, and the W-E maximum horizontal stress (σ_1) causing dextral strike-slip of the longitudinal faults with reverse dip component (transpression). The dashed lines on M1 and M2 planes indicate the top of the fault.

earthquake of magnitude 5.8, as is the case of M2, in which our kinematic inversion results suggest a fault with an approximate rupture area of 11 × 9 km, being more plausible scenario B. Likewise, this fault is oblique to AFS and probably produces the southern pattern in L. Based on their dimensions, this fault is unlikely to generate earthquakes greater than 4.9, according to the relations of Wells and Coppersmith (1994) for a transcurrent fault.

The Ucrania and La Florida faults (Chicangana-Montón et al., 2022) are the northwestern and southeastern borders of a regional restraining bend with a positive flower structure where the Mesetas sequence is located (Figure 10c). The orientation of the principal stresses (σ1 azimuth/plunge = 88°/4°, σ2 = 350°/61°, σ3 = 180°/29°) and OOFs characterized by s/d/r = 232°/63°/168° and 305°/69°/21° of Mesetas seismicity coincide with this transpressive environment (Figure 10b). The Mesetas doublet is schematized by the interaction of two structural styles: duplex and domino, generated by transpressive regional tectonics where AFS is the main system. We also remark that the differences between the theoretical (Figure 10b) and mapped (Figure 10c) models are due to ancient fractures of the massif, reactivated during the latest Andean episode, under the present-day stress field (e.g., García-Delgado et al., 2022). Furthermore, the optimal orientation of faults (OOFs) is probably related to the orientation of the minor Riedels related to duplex and domino styles (Figure 10b).

This interpretation is supported by the resulting L-shaped relocation of aftershocks recorded by the regional seismic network (Figures 4 and 10c), where the cluster observed connects the AFS (northern part of L-arm) with an orthogonal fault in the domino-style (southern part of the L-arm). The kinematic inversion results, with M1 rupturing on the plane of at 210° and dipping 70° (from CMT results) and M2 on the plane of 197° and dipping 70° (scenario B) supported by the results of Coulomb stress modeling (Figure 9) suggest that M1 and M2 are located within the Algeciras fault. Therefore, it is likely that the southern part of the L-pattern was triggered on the orthogonal fault system in the domino style, where minor faults with sinistral kinematics are located. The moment tensor and tectonic stress solutions show principal stress σ_1 of azimuth/plunge = 88°/4° (Figures 3d and 10c), this result is roughly in agreement with local transpressive stress regime in this area (Arcila & Muñoz–Martín, 2019; García-Delgado et al., 2022). The occurrence of the Mesetas mainshocks on two closely spaced faults is explained in terms of the duplex style along a restraining bend zone and fit into the regional frame of transpressive tectonics (Figure 10a).

8. Conclusions

The 2019 Mesetas doublet (Mw 6.0 and 5.8, separated by a few kilometers and 16 min) and the associated aftershock sequence occurred at shallow depths (5–20 km) on two nearly parallel right-lateral strike-slip faults with a reverse component (strike ~ 200°, dip ~ 70°, rake ~ 150°). Both were close to one of the OOFs existing in the local stress field that is characterized by the following azimuths/plunges of principal axes: σ_1 = 88°/4°, σ_2 = 350°/61°, σ_3 = 180°/29°, and stress shape ratio of 0.56. Both mainshocks ruptured basically upward and in the northeast direction relative to their hypocenters, with peak slips of approximately 0.4 and 0.25 m, respectively. The activated rupture planes, oblique to the dominant strike of the major AFS, can be explained in terms of the duplex style along a restraining bend zone and fit into the regional frame of transpressive tectonics. The proposed source characteristics imply that deterministic models for hazard assessment in the megacity of Bogotá should consider active structures possibly deviating from the known major faults and involving complexities (multiple faults). In this work, it was possible to observe some minor faults that coincide with geomorphic and seismological observations. In particular, a minor fault in the domino style agrees with the southern arm of the seismic sequence. This fault is oblique to the AFS (southern part of the L-arm) in the domino style (Figure 10).

Data Availability Statement

Waveform data in miniSEED format (https://ds.iris.edu/ds/nodes/dmc/data/formats/miniseed/) can be downloaded by querying the FDSN web service of Servicio Geológico Colombiano (SGC) at http://sismo.sgc.gov.co:8080/fdsnws/dataselect/1/builder. An example of the request can be made as follows: http://sismo.sgc.gov.co:8080/fdsnws/dataselect/1/query?starttime=2019-12-24T14:21:59%26endtime=2019-12-24T14:28:59%26network=CM%26sta=BRJC%26cha=*%26loc=*%26format=miniseed%26nodata=404. Furthermore, It is possible to download the waveforms by using ObsPy (Beyreuther et al., 2010), for more information see https://docs.obspy.org/packages/obspy.clients.fdsn.html. The LinSlipInv code (Gallovič et al., 2015) to perform kinematic inversion is available on GitHub https://github.com/fgallovic and licensed under GNU GPLv3. The moment tensor solutions were calculated using ISOLA code (Zahradník & Sokos, 2018) available at http://geo.mff.cuni.cz/~jz/for_ISOLAnews. The *b*-value and magnitude of completeness were calculated using the ZMAP code available on GitHub https://github.com/swiss-seismological-service/zmap7. To characterize the compressive stress orientations, we used the StressInverse code (Vavryčuk, 2014), available at https://www.ig.cas.cz/en/stress-inverse/. Figures were created using GMT 5.4.5 (https://github.com/GenericMappingTools/gmt/releases/tag/5.4.5).

Acknowledgments
The Colombian government supported the present study through the Servicio Geológico Colombiano (SGC). This study was funded by the SGC through the project "Evaluación y Monitoreo de la Actividad sísmica". The authors are especially grateful to Hans Agurto-Detzel, Franck Audemard, Isabelle Manighetti, James Kellogg, the anonymous reviewers and editor of ESS (Graziella Caprarelli), whose comments and suggestions helped improve the original version. The authors want to express their gratitude to the Red Sismológica Nacional de Colombia (RSNC) team for generously providing the data for conducting this study.

References

Acevedo, A. B., Yepes-Estrada, C., González, D., Silva, V., Mora, M., Arcila, M., & Posada, G. (2020). Seismic risk assessment for the residential buildings of the major three cities in Colombia: Bogotá, Medellín, and Cali. *Earthquake Spectra*, *36*(2), 298–320. https://doi.org/10.1177/8755293020942537

Alvarado, A., Audin, L., Nocquet, J. M., Jaillard, E., Mothes, P., Jarrín, P., et al. (2016). Partitioning of oblique convergence in the Northern Andes subduction zone: Migration history and the present-day boundary of the North Andean Sliver in Ecuador. *Tectonics*, *35*(5), 1048–1065. https://doi.org/10.1002/2016TC004117

Arcila, M., & Muñoz–Martín, A. (2019). Integrated perspective of the present–day stress and strain regime in Colombia from analysis of earthquake focal mechanisms and geodetic data. *The Geology of Colombia, Volume 4 Quaternary. Servicio Geológico Colombiano*, *4*, 549–569. https://doi.org/10.32685/pub.esp.38.2019.17

Audemard, F. A., & Castilla, R. (2016). Present-day stress tensors along the southern Caribbean plate boundary zone from inversion of focal mechanism solutions: A successful trial. *Journal of South American Earth Sciences*, *71*, 309–319. https://doi.org/10.1016/j.jsames.2016.06.005

Audemard, F. A., Mora-Páez, H., & Fonseca, H. A. (2021). Net right-lateral slip of the Eastern Frontal Fault System, North Andes Sliver, northwestern South America. *Journal of South American Earth Sciences*, *109*, 103286. ISSN 0895-9811. https://doi.org/10.1016/j.jsames.2021.103286

Audemard, F. E., & Audemard, F. A. (2002). Structure of the Mérida Andes, Venezuela: Relations with the South America–Caribbean geodynamic interaction. *Tectonophysics*, *345*(1–4), 1–26. https://doi.org/10.1016/S0040-1951(01)00218-9

Beyreuther, M., Barsch, R., Krischer, L., Megies, T., Behr, Y., & Wassermann, J. (2010). ObsPy: A Python toolbox for seismology. *Seismological Research Letters*, *81*(3), 530–533. https://doi.org/10.1785/gssrl.81.3.530

Cediel, F., Shaw, R., & Cáceres, C. (2003). Tectonic assembly of the Northern Andean block. *The Circum-Gulf of Mexico and the Caribbean: Hydrocarbon Habitats, Basin Formation, and Plate Tectonics*, *79*, 815–848.

Chicangana-Montón, G., Bocanegra-Gómez, A., Pardo-Mayorga, J., Salcedo-Hurtado, J., Gómez-Capera, A., & Vargas-Jiménez, C. A. (2022). Sismicidad y sismotectónica para el sector norte del ámbito del Sistema de Fallas de Algeciras, Cordillera Oriental, Colombia. *Boletin de Geologia*, *44*(1), 111–134. https://doi.org/10.18273/revbol.v44n1-2022005

Cifuentes, H., & Sarabia, M. (2009). *Revisión de información histórica y reevaluación de intensidades del sismo del 9 de febrero de 1967, Colombia (Huila)*. Bogotá.

Constable, S. C., Parker, R. L., & Constable, C. G. (1987). Occam's inversion: A practical algorithm for generating smooth models from electromagnetic sounding data. *Geophysics*, *52*(3), 289–300. https://doi.org/10.1190/1.1442303

Das, S., & Henry, C. (2003). Spatial relation between main earthquake slip and its aftershock distribution. *Reviews of Geophysics*, *41*(3), 1013. https://doi.org/10.1029/2002RG000119

Dicelis, G., Assumpção, M., Kellogg, J., Pedraza, P., & Dias, F. (2016). Estimating the 2008 Quetame (Colombia) earthquake source parameters from seismic data and InSAR measurements. *Journal of South American Earth Sciences*, *72*, 250–265. https://doi.org/10.1016/j.jsames.2016.09.011

Diederix, H., Bohórquez, O. P., Mora–Páez, H., Peláez, J. R., Cardona, L., Corchuelo, Y., et al. (2020). The Algeciras Fault System of the Upper Magdalena Valley, Huila department. In J. Gómez & A. O. Pinilla–Pachon (Eds.), *The Geology of Colombia, Volume 4 Quaternary* (Vol. 38, pp. 423–452). Servicio Geológico Colombiano, Publicaciones Geológicas Especiales. https://doi.org/10.32685/pub.esp.38.2019.12

Diederix, H., Bohórquez-Orozco, O., Gómez-Hurtado, E., Idárraga-García, J., Rendón-Rivera, A., Audemard, F., & Mora-Páez, H. (2021). Paleoseismologic trenching confirms recent Holocene activity of the major Algeciras Fault System in southern Colombia. *Journal of South American Earth Sciences*, *109*, 103263. https://doi.org/10.1016/j.jsames.2021.103263

Dimaté, C., Rivera, L., & Cisternas, A. (2005). Re-visiting large historical earthquakes in the Colombian Eastern Cordillera. *Journal of Seismology*, *9*(1), 1–22. https://doi.org/10.1007/s10950-005-1413-2

Dziewonski, A. M., Chou, T. A., & Woodhouse, J. H. (1981). Determination of earthquake source parameters from waveform data for studies of global and regional seismicity. *Journal of Geophysical Research*, *86*(B4), 2825–2852. https://doi.org/10.1029/JB086iB04p02825

Egbue, O., & Kellogg, J. N. (2010). Pleistocene to present North Andean "escape". *Tectonophysics*, *489*(1–4), 248–257. https://doi.org/10.1016/j.tecto.2010.04.021

Ekström, G., Nettles, M., & Dziewonski, A. M. (2021). The global CMT project 2004–2010: Centroid-moment tensors for 13,017 earthquakes. *Physics of the Earth and Planetary Interiors*, *200–201*, 1–9. https://doi.org/10.1016/j.pepi.2012.04.002

Escalona, A., & Mann, P. (2011). Tectonics, basin subsidence mechanisms, and paleogeography of the Caribbean-South American plate boundary zone. *Marine and Petroleum Geology*, *28*(1), 8–39. https://doi.org/10.1016/j.marpetgeo.2010.01.016

Fojtíková, L., & Vavryčuk, V. (2018). Tectonic stress regime in the 2003–2004 and 2012–2015 earthquake swarms in the Ubaye Valley, French Alps. *Pure and Applied Geophysics*, *175*(6), 1997–2008. https://doi.org/10.1007/s00024-018-1792-2

Frohlich, C., & Davis, S. D. (1993). Teleseismic b values; Or, much ado about 1.0. *Journal of Geophysical Research*, *98*(B1), 631–644. https://doi.org/10.1029/92JB01891

Gallovič, F. (2015). Modeling velocity recordings of the Mw 6.0 South Napa, California, earthquake: Unilateral event with weak high-frequency directivity. *Seismological Research Letters*, *87*(1), 2–14. https://doi.org/10.1785/0220150042

Gallovič, F., Imperatori, W., & Mai, P. M. (2015). Effects of three-dimensional crustal structure and smoothing constraint on earthquake slip inversions: Case study of the Mw 6.3 2009 L'Aquila earthquake. *Journal of Geophysical Research: Solid Earth*, *120*(1), 428–449. https://doi.org/10.1002/2014JB011650

Gallovič, F., & Zahradník, J. (2011). Toward understanding slip inversion uncertainty and artifacts: 2. Singular value analysis. *Journal of Geophysical Research*, *116*(B2), B02309. https://doi.org/10.1029/2010JB007814

García-Delgado, H., Velandia, F., Bermúdez, M. A., & Audemard, F. A. (2022). The present-day tectonic regimes of the Colombian Andes and the role of slab geometry in intraplate seismicity. *International Journal of Earth Scinces (Geol Rundsch)*, *111*(7), 1–19. https://doi.org/10.1007/s00531-022-02227-9

Gutscher, M.-A., Spakman, W., Bijwaard, H., & Engdahl, E. R. (2000). Geodynamics of flat subduction: Seismicity and tomographic constraints from the Andean margin. *Tectonics*, *19*(5), 814–833. https://doi.org/10.1029/1999TC001152

Kellogg, J. N., Camelio, G. B. F., & Mora-Páez, H. (2019). Cenozoic tectonic evolution of the North Andes with constraints from volcanic ages, seismic reflection, and satellite geodesy. In *Andean tectonics* (pp. 69–102). Elsevier. https://doi.org/10.1016/B978-0-12-816009-1.00006-X

Kellogg, J. N., Vega, V., Stailings, T. C., Aiken, C. L. V., & Kellogg, J. N. (1995). Tectonic development of Panama, Costa Rica, and the Colombian Andes: Constraints from global positioning system geodetic studies and gravity. In *Geologic and tectonic development of the Caribbean plate boundary in Southern Central America, Paul Mann*.

Kim, Y., Peacock, D., & Sanderson, D. (2004). Fault damage zones. *Journal of Structural Geology*, *26*(3), 503–517. https://doi.org/10.1016/j.jsg.2003.08.002

Lomax, A., Virieux, J., Volant, P., & Berge-Thierry, C. (2000). Probabilistic earthquake location in 3D and layered models. In C. H. Thurber & N. Rabinowitz (Eds.), *Advances in Seismic event location*, *Modern approaches in geophysics* (Vol. 18, pp. 101–134). Springer. https://doi.org/10.1007/978-94-015-9536-0_5

Mai, P. M., Schorlemmer, D., Page, M., Ampuero, J., Asano, K., Causse, M., et al. (2016). The earthquake-source inversion validation (SIV) project. *Seismological Research Letters*, *87*(3), 690–708. https://doi.org/10.1785/0220150231

Mann, P. (2007). Global catalogue, classification and tectonic origins of restraining and releasing bends on active and ancient strike-slip fault systems. In W. Cunningham & P. Mann (Eds.), *Tectonics of strike-slip restraining and releasing bends* (pp. 13–142). Geological Society of London. Special Publications 290.

Montes, C., Hatcher, R. D., & Restrepo-Pace, P. A. (2005). Tectonic reconstruction of the northern Andean blocks: Oblique convergence and rotations derived from the kinematics of the Piedras–Girardot area, Colombia. *Tectonophysics*, *399*(1–4), 221–250. https://doi.org/10.1016/j.tecto.2004.12.024

Mora, A., & Parra, M. (2008). The structural style of footwall shortcuts along the eastern foothills of the Colombian Eastern Cordillera. Differences with other inversion related structures. *CTyF - Ciencia, Tecnología Y Futuro. scieloco.*, *3*(4), 7–21. https://doi.org/10.29047/01225383.460

Mora, A., Reyes-Harker, A., Rodríguez, G., Tesón, E., Ramírez-Arias, J. C., Parra, M., et al. (2013). Inversion tectonics under increasing rates of shortening and sedimentation: Cenozoic example from the Eastern Cordillera of Colombia. *Geological Society of London Special Publications*, *377*(1), 411–442. https://doi.org/10.1144/SP377.6

Mora-Páez, H., Kellogg, J. N., Freymueller, J. T., Mencin, D., Fernandes, R. M. S., Diederix, H., et al. (2019). Crustal deformation in the Northern Andes—A new GPS velocity field. *Journal of South American Earth Sciences*, *89*, 76–91. https://doi.org/10.1016/j.jsames.2018.11.002

Nocquet, J.-M., Villegas-Lanza, J. C., Chlieh, M., Mothes, P. A., Rolandone, F., Jarrin, P., et al. (2014). Motion of continental slivers and creeping subduction in the Northern Andes. *Nature Geoscience*, *7*(4), 287–291. https://doi.org/10.1038/ngeo2099

Noisagool, S., Boonchaisuk, S., Pornsopin, P., & Siripunvaraporn, W. (2016). The regional moment tensor of the 5 May 2014 Chiang Rai earthquake (Mw = 6.5), Northern Thailand, with its aftershocks and its implication to the stress and the instability of the Phayao Fault Zone. *Journal of Asian Earth Sciences*, *127*, 231–245. https://doi.org/10.1016/j.jseaes.2016.06.008

Noriega-Londoño, S., Bermúdez, M. A., Restrepo-Moreno, S. A., Marín-Cerón, M. I., & García-Delgado, H. (2021). Earthquake ground deformation using DInSAR analysis and instrumental seismicity: The 2019 M 6.0 Mesetas Earthquake, Meta, Colombian Andes. *Boletín de la Sociedad Geológica Mexicana*, *73*(2), A090221. https://doi.org/10.18268/BSGM2021v73n2a090221

Parsons, T., Stein, R. S., Simpson, R. W., & Reasenberg, P. A. (1999). Stress sensitivity of fault seismicity: A comparison between limited-offset oblique and major strike-slip faults. *Journal of Geophysical Research*, *104*(B9), 20183–20202. https://doi.org/10.1029/1999JB900056

Pedraza, P., & Pulido, N. (2018). *Minimum 1D seismic velocity model from local earthquakes data in Servitá Fault System, Eastern Cordillera of Colombia*. Servicio Geológico Colombiano.

Pennington, W. D. (1981). Subduction of the eastern Panama basin and seismotectonics of northwestern South America. *Journal of Geophysical Research*, *86*(B11), 10753–10770. https://doi.org/10.1029/JB086iB11p10753

Pizzi, A., Di Domenica, A., Gallovič, F., Luzi, L., & Puglia, R. (2017). Fault segmentation as constraint to the occurrence of the main shocks of the 2016 Central Italy seismic sequence. *Tectonics*, *36*(11), 2370–2387. https://doi.org/10.1002/2017TC004652

Poveda, E., Julià, J., Schimmel, M., & Perez-Garcia, N. (2018). Upper and middle crustal velocity structure of the Colombian Andes from ambient noise tomography: Investigating subduction-related Magmatism in the overriding plate. *Journal of Geophysical Research: Solid Earth*, *123*(2), 1459–1485. https://doi.org/10.1002/2017JB014688

Ragon, T., Sladen, A., & Simons, M. (2018). Accounting for uncertain fault geometry in earthquake source inversions—I: Theory and simplified application (2018). *Geophysical Journal International*, *214*(2), 1174–1190. https://doi.org/10.1093/gji/ggy187

Riaño, A. C., Reyes, J. C., Yamín, L. E., Bielak, J., Taborda, R., & Restrepo, D. (2021). Integration of 3D large-scale earthquake simulations into the assessment of the seismic risk of Bogota, Colombia. *Earthquake Engineering & Structural Dynamics*, *50*(1), 155–176. https://doi.org/10.1002/eqe.3373

Sambridge, M., Gallagher, K., Jackson, A., & Rickwood, P. (2006). Trans-dimensional inverse problems, model comparison and the evidence. *Geophysical Journal International*, *167*(2), 528–542. https://doi.org/10.1111/j.1365-246X.2006.03155.x

Singh, S. C., Hananto, N., Qin, Y., Leclerc, F., Avianto, P., Tapponnier, P. E., et al. (2017). The discovery of a conjugate system of faults in the Wharton Basin intraplate deformation zone. *Science Advances*, *3*(1), e1601689. https://doi.org/10.1126/sciadv.1601689

Somerville, P., Irikura, K., Graves, R., Sawada, S., Wald, D., Abrahamson, N., et al. (1999). Characterizing crustal earthquake slip models for the prediction of strong ground motion. *Seismological Research Letters*, *70*(1), 59–80. https://doi.org/10.1785/gssrl.70.1.59

Spikings, R., Cochrane, R., Villagomez, D., Lelij, R. V. D., Vallejo, C., Winkler, W., & Beate, B. (2015). The geological history of northwestern South America: From Pangaea to the early collision of the Caribbean large igneous Province (290–75 Ma). *Gondwana Research*, *27*(1), 95–139. https://doi.org/10.1016/j.gr.2014.06.004

Styron, R., & Pagani, M. (2020). The GEM global active faults database. *Earthquake Spectra*, *36*, 160–180. https://doi.org/10.1177/8755293020944182

Suárez, G., Molnar, P., & Burchfiel, B. C. (1983). Seismicity, fault plane solutions, depth of faulting, and active tectonics of the Andes of Peru, Ecuador, and southern Colombia. *Journal of Geophysical Research*, *88*(B12), 10403–10428. https://doi.org/10.1029/JB088iB12p10403

Taboada, A., Rivera, L. A., Fuenzalida, A., Cisternas, A., Philip, H., Bijwaard, H., et al. (2000). Geodynamics of the Northern Andes: Subductions and intracontinental deformation (Colombia). *Tectonics*, *19*(5), 787–813. https://doi.org/10.1029/2000TC900004

Toda, S., Stein, R. S., Sevilgen, V., & Lin, J. (2011). Coulomb 3.3 Graphic-rich deformation and stress-change software for earthquake, tectonic, and volcano research and teaching—user guide. Retrieved from https://pubs.usgs.gov/of/2011/1060/

Trenkamp, R., Kellogg, J. N., Freymueller, J. T., & Mora, H. P. (2002). Wide plate margin deformation, southern Central America and northwestern South America, CASA GPS observations. *Journal of South American Earth Sciences*, *15*(2), 157–171. https://doi.org/10.1016/S0895-9811(02)00018-4

Vallée, M., & Douet, V. (2016). A new database of source time functions (STFs) extracted from the SCARDEC method. *Physics of the Earth and Planetary Interiors*, *257*, 149–157. ISSN 0031-9201. https://doi.org/10.1016/j.pepi.2016.05.012

van der Elst, N. J., & Shaw, B. E. (2015). Larger aftershocks happen farther away: Nonseparability of magnitude and spatial distributions of aftershocks. *Geophysical Research Letters*, *42*(14), 5771–5778. https://doi.org/10.1002/2015GL064734

Vargas, C. A., Gomez, J. S., Gomez, J. J., Solano, J. M., & Caneva, A. (2021). Comment on seismic electric signals (SES) and earthquakes: A review of an updated VAN method and competing hypotheses for SES generation and earthquake triggering by Daniel S. Helman, physics of Earth and planetary interiors, 302 (2020). *Physics of the Earth and Planetary Interiors*, *313*, 106676. https://doi.org/10.1016/j.pepi.2021.106676

Vavryčuk, V. (2011). Principal earthquakes: Theory and observations from the 2008 west Bohemia swarm. *Earth and Planetary Science Letters*, *305*(3–4), 290–296. https://doi.org/10.1016/j.epsl.2011.03.002

Vavryčuk, V. (2014). Iterative joint inversion for stress and fault orientations from focal mechanisms. *Geophysical Journal International*, *199*(1), 69–77. https://doi.org/10.1093/gji/ggu224

Velandia, F., Acosta, J., Terraza, R., & Villegas, H. (2005). The current tectonic motion of the Northern Andes along the Algeciras Fault System in SW Colombia. *Tectonophysics*, *399*(1–4), 313–329. https://doi.org/10.1016/j.tecto.2004.12.028

Veloza, G., Styron, R., Taylor, M., & Mora, A. (2012). Open-source archive of active faults for northwest South America. *Geological Society of America Today*, *22*(10), 4–10. https://doi.org/10.1130/GSAT-G156A.1

Wahba, G., & Craven, P. (1978). Smoothing Noisy data with spline functions. Estimating the Correct degree of smoothing by the method of generalized cross-validation. *Numerische Mathematik*, *31*(4), 377–404. https://doi.org/10.1007/bf01404567

Waldhauser, F., & Ellsworth, W. (2000). A double-difference earthquake location algorithm: Method and application to the Northern Hayward fault, California. *Bulletin of the Seismological Society of America*, *90*(6), 1353–1368. https://doi.org/10.1785/0120000006

Wells, D., & Coppersmith, K. (1994). New empirical relationships among magnitude, rupture length, rupture width, rupture area, and surface displacement. *Bulletin of the Seismological Society of America*, *84*(4), 974–1002. https://doi.org/10.1785/BSSA0840040974

Wetzler, N., Lay, T., Brodsky, E. E., & Kanamori, H. (2018). Systematic deficiency of aftershocks in areas of high coseismic slip for large subduction zone earthquakes. *Science Advances*, *4*(2), eaao3225. https://doi.org/10.1126/sciadv.aao3225

Wiemer, S. (2001). A software package to analyze seismicity: ZMAP. *Seismological Research Letters*, *72*(3), 373–382. https://doi.org/10.1785/gssrl.72.3.373

Woodcock, N., & Schubert, C. (1994). Continental strike-slip tectonics. In P. Hancock (Ed.), *Continental deformation* (pp. 251–263). Pergamon Press.

Yáñez-Cuadra, V., Ortega-Culaciati, F., Moreno, M., Tassara, A., Krumm-Nualart, N., Ruiz, J., et al. (2022). Interplate coupling and seismic potential in the Atacama seismic gap (Chile): Dismissing a rigid Andean sliver. *Geophysical Research Letters*, *49*(11), e2022GL098257. https://doi.org/10.1029/2022GL098257

Zahradník, J., & Gallovič, F. (2010). Toward understanding slip inversion uncertainty and artifacts. *Journal of Geophysical Research*, *115*(B9), B09310. https://doi.org/10.1029/2010JB007414

Zahradník, J., & Sokos, E. (2018). ISOLA code for multiple-point source modeling review (pp. 1–28). https://doi.org/10.1007/978-3-319-77359-9_1